Bifurcation-based micro-/nanoelectromechanical mass detection

van Nghi Nguyen, Sébastien Baguet, Claude-Henri Lamarque, Régis Dufour

▶ **To cite this version:**

van Nghi Nguyen, Sébastien Baguet, Claude-Henri Lamarque, Régis Dufour. Bifurcation-based micro-/nanoelectromechanical mass detection. Nonlinear Dynamics, 2015, 79 (1), pp.647-662. 10.1007/s11071-014-1692-7 . hal-01066276

HAL Id: hal-01066276
https://hal.science/hal-01066276

Submitted on 26 Sep 2014

HAL is a multi-disciplinary open access archive for the deposit and dissemination of scientific research documents, whether they are published or not. The documents may come from teaching and research institutions in France or abroad, or from public or private research centers.

L'archive ouverte pluridisciplinaire **HAL**, est destinée au dépôt et à la diffusion de documents scientifiques de niveau recherche, publiés ou non, émanant des établissements d'enseignement et de recherche français ou étrangers, des laboratoires publics ou privés.

Produit par HAL - 16 Sep 2014

Nonlinear Dyn - Author's accepted manuscript
The final publication is available at Springer via http://dx.doi.org/10.1007/s11071-014-1692-7

Bifurcation-based micro/nano-electromechanical mass detection

V-N. Nguyen · S. Baguet · C-H. Lamarque · R. Dufour

Received: date / Accepted: date

Abstract This paper investigates an alternative mass sensing technique based on nonlinear micro/nanoelectromechanical resonant sensors. The proposed approach takes advantage of multi-stability and bifurcations of the hysteretic frequency responses of the electrostatically-actuated resonator. For this purpose, a reduced-order model is considered. Numerical results show that sudden jumps in amplitude make the detection of a very small mass possible. Moreover, the limit of detection can be set with the value of the operating frequency. However, when operating at fixed frequency, the study of basins of attraction indicates that this bifurcation-based mass detection does not exhibit the expected robustness. A possible improvement is proposed, based on the reinitialization of the system by a forced jump-down on the hysteretic response curve. Using a frequency sweep which varies slowly in sinusoidal form solves the reinitialization problem and enables automatic real-time detection. Finally the added mass is located on the beam by using the resonance at the first two natural frequencies.

Keywords N/MEMS · mass sensing · nonlinear dynamics · basin of attraction · bifurcation · detection · quantification · localization

V-N. Nguyen · S. Baguet · R. Dufour
Université de Lyon, CNRS, INSA-Lyon, LaMCoS UMR5259, F-69621 Villeurbanne, France
E-mail: van-nghi.nguyen@insa-lyon.fr
E-mail: Sebastien.Baguet@insa-lyon.fr
E-mail: Regis.Dufour@insa-lyon.fr

C-H. Lamarque
Université de Lyon, CNRS
ENTPE/LGCB et LTDS, UMR5513, F-69518 Vaulx-en-Velin, France
E-mail: Claude.Lamarque@entpe.fr

1 Introduction

Measuring tiny masses is an important application of M/NEMS resonant sensors. Mass sensors are used in biologic environment for DNA hybridization, biomolecules, enzymes, proteins [1,2,3], chemical reactions [4], mercury's vapor [5,6,7], gas concentration [8], explosives [9], etc.

Generally speaking, the principle of a resonant sensor is based on the forcing of a microbeam on its fundamental bending mode by means of an electrode which can also serve as a detection sensor of the frequency shift induced by an external perturbation (added mass, acceleration, Coriolis force [10]). The size of the sensor is conditioned by the mass to be detected. The dynamic range can theoretically be improved by downsizing the sensors. However, downsizing is limited by available manufacturing processes, by the need of detection surfaces as large as possible, and by the onset of undesirable non-linear phenomena. A length of 150 nm associated with a forcing frequency of 2 GHz makes a 1.7 yg ($1yg = 10^{-24}g$) mass detection possible, see Chaste et al. [11], while a length of 4 μm limits the detection to a 0.4 ag ($1ag = 10^{-18}g$) [12]. Hanay et al. [13] studied the potential of NEMS-based mass spectrometry (NEMS-MS) by measuring the mass of an individual protein macromolecules in real time. Such a NEMS-MS system can access masses above 500kDa (1Da=1.66 $\times 10^{-27}kg$) and has a sensitivity of a single Dalton and an upper limit of detection of hundreds of MegaDaltons [14]. In [12], the theoretical and experimental fundamental frequency shifts are compared. It is shown that the relation between frequency shift and added mass is linear, i.e the smaller the added mass is, the smaller the frequency shift is.

Several techniques have been explored to enhance the sensitivity. The resonator can be driven in linear or nonlinear regime. In the linear regime [12], vibrations are limited to small amplitudes which may not exceed thermo-mechanical

noise, thus making the detection difficult. Exciting the microbeam in the non-linear regime can improve the sensitivity of detection, as shown by Buks and Yurke [15] [16], but exposes the resonator to pull-in, namely the collapse of the moving structure onto the fixed electrode [17] [18] [19]. Another possibility consists in using higher modes. Narducci et al. [20] studied the first two modes of a beam and showed experimentally that the sensitivity is higher for the second resonance frequency than for the fundamental one. In [21], the sensitivity of detection is improved from 23 to 276 times when switching from the second to the fourth mode. However, exciting higher modes requires much more energy than for the fundamental mode to obtain the same output signal amplitude. Using the first torsional mode of microcantilevers rather than the first bending mode can also improve the resolution by one order [22][23]. Parametrically excited mechanical systems have also attracted attention [24]. Zhang et al. [25,26] concluded that if the resonator is parametrically excited, its sensitivity is highly increased. Similarly, in [27], Thomas et al. achieved experimentally a quality factor enhancement by up to a factor 14 in air by means of parametric amplification.

Recent research has developed alternative sensing approaches exploiting inherent properties of the non-linear behavior of MEMS like dynamic instabilities or bi-stability, and based on amplitude rather than frequency shifts. Khater et al. [28] showed that the sensitivity of electrostatically actuated MEMS is highly enhanced when the sensor is operated close to pull-in. They proposed a binary sensing mechanism in which the sensor goes to pull-in when the mass to detect exceeds a given threshold. In [29], Younis et al. observed that exciting a electrostatically actuated microbeam close twice its fundamental frequency is very attractive as it provides a sharp transition from the no-mass to the added-mass response curve.

Very recently, Kumar et al. [30,31] proposed a bifurcation-based mass sensing technique and explained the use of amplitude jumps between multi-stable states close to a cyclic-fold/saddle-node bifurcation in the non-linear frequency response. Harne and Wang [32] presented a bifurcation-based coupled linear-bistable system for mass sensing, providing experimental results of bifurcations between multi-stable states. In [33], Guo and Fedder introduced the use of hysteretic cycle in the frame of a bi-state control of a parametric resonance.

In this paper, similar ideas are discussed and improved taking into account dynamical bifurcations and transient behaviors in hysteretic cycles. Strategies for detection, quantification and localization of an added mass are proposed. Section 2 presents the model, Section 3 the principle of detection, Section 4 the quantification and Section 5 the localization.

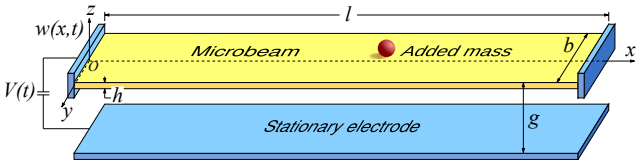

Fig. 1 Schematic of the clamped-clamped microbeam-based electromechanical resonator

2 Model

To describe the principles of detection, quantification and localization of a small added mass, a model of a clamped-clamped beam is studied with or without added mass. The model considered here permits developing orders of magnitude of realistic beams. These developments could be extended to other models.

2.1 Case without added mass

Let the clamped-clamped beam model sketched in Fig. 1, have its nonlinear behavior in bending governed by the integro-differential equation [34], [35]:

$$EI\frac{\partial^4\tilde{w}(\tilde{x},\tilde{t})}{\partial\tilde{x}^4}+\rho bh\frac{\partial^2\tilde{w}(\tilde{x},\tilde{t})}{\partial\tilde{t}^2}+\tilde{c}\frac{\partial\tilde{w}(\tilde{x},\tilde{t})}{\partial\tilde{t}} - \left[\tilde{N}+\frac{Ebh}{2l}\int_0^l\left(\frac{\partial\tilde{w}(\tilde{x},\tilde{t})}{\partial\tilde{x}}\right)^2\mathrm{d}\tilde{x}\right]\frac{\partial^2\tilde{w}(\tilde{x},\tilde{t})}{\partial\tilde{x}^2} = \frac{1}{2}\varepsilon_0\frac{bC_n\left(V_{dc}+V_{ac}\cos\tilde{\Omega}\tilde{t}\right)^2}{(g-\tilde{w}(\tilde{x},\tilde{t}))^2}, \quad (1)$$

with $\tilde{w}(\tilde{x},\tilde{t})$ the lateral deflexion of the beam along the axis Ox, I,h,b and l the moment of inertia, thickness, height, and length of the beam respectively, E and ρ the modulus of elasticity and the mass density of the material, $\tilde{c}$ the viscous damping coefficient, g the beam-electrode gap. The axial force $\tilde{N}$ is due to design and manufacturing, and the bias V_{dc} and alternative V_{ac} voltages to the electrode. The coefficient C_n related to fringing field effect is computed in [36]. By using nondimensional variables, Eq. (1) becomes:

$$\frac{\partial^4 w(x,t)}{\partial x^4}+\frac{\partial^2 w(x,t)}{\partial t^2}+c\frac{\partial w(x,t)}{\partial t} - \left[N+\alpha_1\int_0^1\left(\frac{\partial w(x,t)}{\partial x}\right)^2\mathrm{d}x\right]\frac{\partial^2 w(x,t)}{\partial x^2} = \alpha_2\frac{\left(V_{dc}+V_{ac}\cos\Omega t\right)^2}{(1-w(x,t))^2}, \quad (2)$$

Produit par HAL - 16 Sep 2014

Produit par HAL - 16 Sep 2014

where

$$w=\frac{\tilde{w}}{g},\quad x=\frac{\tilde{x}}{l},\quad t=\frac{\tilde{t}}{\tau}$$
$$N=\frac{\tilde{N}l^2}{EI},\quad \alpha_1=6\big(\frac{g}{h}\big)^2,\quad \alpha_2=6C_n\frac{\varepsilon_0 l^4}{Eh^3g^3} \tag{3}$$
$$\tau=\frac{2l^2}{h}\sqrt{\frac{3\rho}{E}};\ \Omega=\tilde{\Omega};\ c=\frac{\tilde{c}l^4}{EI\tau};\ \tilde{c}=\rho bh\frac{\omega_1}{\tau Q}$$

ω_1 and Q are the fundamental frequency and its associated quality factor. The eigenmodes of the linear undamped and unloaded microbeam $\phi_k(x)$ are calculated and the following Galerkin expansion is used for the displacement $w(x,t)$:

$$w(x,t)=\sum_{k=1}^{N_m}\phi_k(x)a_k(t), \tag{4}$$

where $a_k(t)$ is the k^{th} time varying generalized coordinate. Then, Eq. (2) is multiplied by $(1-w(x,t))^2\phi_i(x)$ for $i=1,\ldots,N_m$ and integrated from 0 to 1, and the second-order differential equation in time is written in the form of the matrix equation:

$$\begin{aligned}\big[\mathbf{M}_0+\mathbf{M}_1(\mathbf{a})+\mathbf{M}_2(\mathbf{a})\big]\ddot{\mathbf{a}}+\big[\mathbf{C}_0+\mathbf{C}_1(\mathbf{a})+\mathbf{C}_2(\mathbf{a})\big]\dot{\mathbf{a}}\\ +\big[K_0+\mathbf{K}_1(\mathbf{a})+\mathbf{K}_2(\mathbf{a})\big]\mathbf{a}-\big(N+\alpha_1T_2(\mathbf{a})\big)\big[\mathbf{K}_T+\\ \mathbf{K}_{T1}(\mathbf{a})+\mathbf{K}_{T2}(\mathbf{a})\big]\mathbf{a}=\alpha_2\big(V_{dc}+V_{ac}\cos\Omega t\big)^2\mathbf{F}.\end{aligned} \tag{5}$$

The matrices $\mathbf{M}_0$, $\mathbf{M}_1(\mathbf{a})$, $\mathbf{M}_2(\mathbf{a})$, $\mathbf{C}_0$, $\mathbf{C}_1(\mathbf{a})$, $\mathbf{C}_2(\mathbf{a})$, $\mathbf{K}_0$, $\mathbf{K}_1(\mathbf{a})$, $\mathbf{K}_2(\mathbf{a})$, $\mathbf{K}_T$, $\mathbf{K}_{T1}(\mathbf{a})$, $\mathbf{K}_{T2}(\mathbf{a})$, the vector $\mathbf{F}$ and the scalar $T_2(\mathbf{a})$ are defined in [35]. In this paper, the quasi-analytical averaging method as well as a numerical procedure based on the Harmonic Balance Method and the Asymptotic Numerical Method (ANM) [37] are used to solve Eq. (2) as explained in [35]. The results of the two methods are similar for small amplitude but the difference is significant for high vibration amplitude vibration. This is due to the basic assumptions of the averaging method, that limit its use to small nonlinearities. In [35], the influence of higher modes is also considered and it is shown that for high vibration amplitudes ($W_{max}>0.5$), the computation must be carried out with several modes.

2.2 Case with added mass

Let the small and lumped added mass of mass m_p and of tiny size fall onto the beam's surface. The beam and the added mass constitute a continuum whose bending behavior is governed by the following equation applied to an infinitesimal volume $\mathrm{d}\tilde{x}$, with $\delta_{\tilde{x}_0}(\tilde{x})$ the Dirac function:

Design	Q	h $[\mu m]$	b $[\mu m]$	l $[\mu m]$	g $[\mu m]$
1	10000	10	10	400	2
2	10000	1.5	1.5	40	0.1

Table 1 Designs 1 and 2 of the clamped-clamped microbeam.

$$\begin{aligned}EI\frac{\partial^4\tilde{w}(\tilde{x},\tilde{t})}{\partial\tilde{x}^4}\mathrm{d}\tilde{x}+\rho bh\frac{\partial^2\tilde{w}(\tilde{x},\tilde{t})}{\partial\tilde{t}^2}\mathrm{d}\tilde{x}+\delta_{\tilde{x}_0}(\tilde{x})m_p\frac{\partial^2\tilde{w}(\tilde{x},\tilde{t})}{\partial\tilde{t}^2}\\ +\tilde{c}\frac{\partial\tilde{w}(\tilde{x},\tilde{t})}{\partial\tilde{t}}\mathrm{d}\tilde{x}-\Big(\tilde{N}+\frac{Ebh}{2l}\int_0^l\Big[\frac{\partial\tilde{w}(\tilde{x},\tilde{t})}{\partial\tilde{x}}\Big]^2\mathrm{d}\tilde{x}\Big)\frac{\partial^2\tilde{w}(\tilde{x},\tilde{t})}{\partial\tilde{x}^2}\mathrm{d}\tilde{x}\\ =\frac{1}{2}\varepsilon_0\frac{bC_n\big[V_{dc}+V_{ac}\cos\tilde{\Omega}\tilde{t}\big]^2}{\big(g-\tilde{w}(\tilde{x},\tilde{t})\big)^2}\mathrm{d}\tilde{x}.\end{aligned} \tag{6}$$

By introducing the nondimensional variables (3), Eq. (6) is written in the form:

$$\begin{aligned}\frac{\partial^4w(x,t)}{\partial x^4}\mathrm{d}x+\frac{\partial^2w(x,t)}{\partial t^2}\mathrm{d}x+\delta_{x_0}(x)m\frac{\partial^2w(x,t)}{\partial t^2}\\ +c\frac{\partial w(x,t)}{\partial t}\mathrm{d}x-\Big(N+\alpha_1\int_0^1\Big[\frac{\partial w(x,t)}{\partial x}\Big]^2\mathrm{d}x\Big)\frac{\partial^2w(x,t)}{\partial x^2}\mathrm{d}x\\ =\alpha_2\frac{\big[V_{dc}+V_{ac}\cos\Omega t\big]^2}{(1-w(x,t))^2}\mathrm{d}x,\end{aligned} \tag{7}$$

with $m=\frac{m_p}{\rho bhl}$ the mass ratio. As in the case without added mass, the Galerkin expansion (4) is used and the new matrix equation contains the additional matrices $\boldsymbol{\mu}_0,\boldsymbol{\mu}_1(\mathbf{a}),\boldsymbol{\mu}_2(\mathbf{a})$:

$$\begin{aligned}\big[\mathbf{M}_0+\mathbf{M}_1(\mathbf{a})+\mathbf{M}_2(\mathbf{a})+\boldsymbol{\mu}_0+\boldsymbol{\mu}_1(\mathbf{a})+\boldsymbol{\mu}_2(\mathbf{a})\big]\ddot{\mathbf{a}}+\\ \big[\mathbf{C}_0+\mathbf{C}_1(\mathbf{a})+\mathbf{C}_2(\mathbf{a})\big]\dot{\mathbf{a}}+\big[K_0+\mathbf{K}_1(\mathbf{a})+\mathbf{K}_2(\mathbf{a})\big]\mathbf{a}\\ -\big(N+\alpha_1T_2(\mathbf{a})\big)\big[\mathbf{K}_T+\mathbf{K}_{T1}(\mathbf{a})+\mathbf{K}_{T2}(\mathbf{a})\big]\mathbf{a}\\ =\alpha_2\big(V_{dc}+V_{ac}\cos\Omega t\big)^2\mathbf{F}.\end{aligned} \tag{8}$$

$\boldsymbol{\mu}_0$, $\boldsymbol{\mu}_1$, $\boldsymbol{\mu}_2$ are determined as follows,with $1\le i,j,k,l\le N_m$:

$$\mu_{0ij}=m\phi_i(x_0)\phi_j(x_0), \tag{9}$$
$$\mu_{1ij}=-2m\sum_{k=1}^{N_m}\Big(\phi_i(x_0)\phi_j(x_0)\phi_k(x_0)\Big)a_k(t), \tag{10}$$
$$\mu_{2ij}=m\sum_{k=1}^{N_m}\sum_{l=1}^{N_m}\Big(\phi_i(x_0)\phi_j(x_0)\phi_k(x_0)\phi_l(x_0)\Big)a_k(t)a_l(t), \tag{11}$$

In the following sections, two microbeam designs and three mass ratios (see Tables 1 and 2) are tested.The location of the added mass is assumed to be known in the sections dedicated to the detection and to the quantification. The forced frequency response curves are computed with the ANM.

3 Detection of the presence of an added mass

3.1 Principle

The detection of added mass is based on the shift of the forced frequency responses. Two methods are possible. The

ratio $m = \frac{m_p}{\rho bhl}$	10^{-4}	5.10^{-5}	10^{-5}
m_p(kg) of Design 1	$9,3.10^{-15}$	$4,6.10^{-15}$	$9,3.10^{-16}$
m_p(kg) of Design 2	$2,1.10^{-17}$	$1,05.10^{-17}$	$2,1.10^{-18}$

Table 2 Nondimensional and physical values of added mass

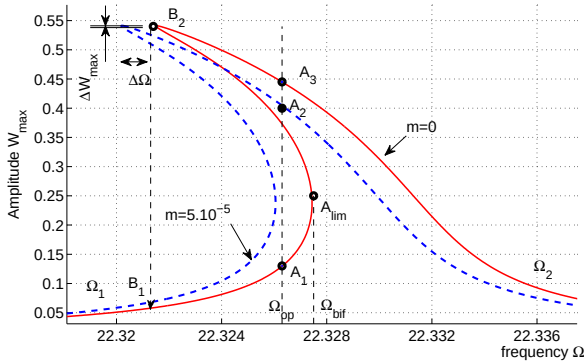

Fig. 2 Design 2: $V_{dc} = 100V_{ac} = 1.9V$, without added mass (solid line), with added mass $m = 5.10^{-5}$ (dashed line)

first one is based on the frequency shift at the maximum of resonance: the presence of the added mass shifts down the forced frequency response, see Fig. 2, $\Delta\Omega$ being the resonant frequency shift. The second one focuses on the amplitude shift ΔW_{max}, see Fig. 2. Unfortunately, at the maximum of resonance, this shift is too small for an accurate detection. In [31], the amplitude shift is measured close to a saddle-node bifurcation instead. This permits to take advantage of the non-linear characteristics of the frequency response and results in a large amplitude jump, thus providing an efficient mass sensing approach. This technique also simplifies the experimental implementation by eliminating the need for complex frequency-tracking hardware [30].

3.2 Softening behavior

Let us consider Design 2 exhibiting a softening behavior. In order to identify the presence of the added mass, the beam is forced at an operating frequency Ω_{op} close to the bifurcation frequency Ω_{bif}. In practice, the frequency is first increased from Ω_1 to Ω_2. When approaching the bifurcation point Ω_{bif}, the frequency is fixed to Ω_{op}. Then, as shown in Fig. 2, the sudden presence of the added mass induces a jump from point A_1 on the solid curve (without added mass) to point A_2 on the dashed curve (with added mass). Fig. 3 shows the forced frequency responses due to two different added masses. A small added mass creates a large jump from A_1 to A_3 and a bigger mass, a smaller jump from A_1 to A_2. Therefore, the smaller the added mass is, the larger the amplitude shift will be.

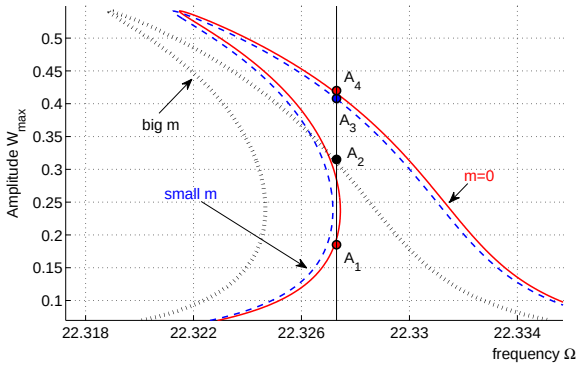

Fig. 3 Design 2: $V_{dc} = 100V_{ac} = 1.9V$, without added mass (solid line), with small added mass (dashed line), with bigger added mass (dotted line)

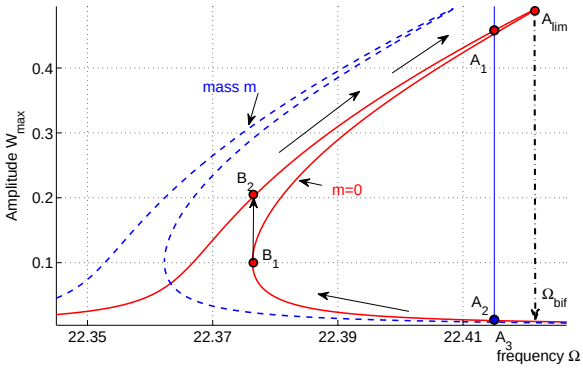

Fig. 4 Design 1: $V_{dc} = 10V_{ac} = 9V$, without added mass (solid line), with added mass (dashed line).

3.3 Hardening behavior

Let us consider Design 1 exhibiting a hardening behavior (see Fig. 4). As for the softening behavior, when approaching the bifurcation frequency Ω_{bif}, the response jumps from a large amplitude at A_1 (solid curve) to a small amplitude at A_2 (dashed curve) with the added mass. This mass is thus detected by the large jump $A_1 \rightarrow A_2$.

3.4 Robustness and reinitialization of detection mechanism

For the softening behavior, with the added mass, the response stabilizes on the periodic limit cycle corresponding to A_2 (see Fig. 2). When the added mass leaves the microbeam, the solution escapes this limit cycle and, after some transient motion, reaches the limit cycle corresponding either to point A1 or to point A3, depending on the initial conditions. If it returns to A_1, the next added mass is easily detected. Conversely, if the solution jumps to the upper point A_3, the next small added mass will cause a small, difficult to detect, jump from A_3 to A_2. The value of the added

Produit par HAL - 16 Sep 2014

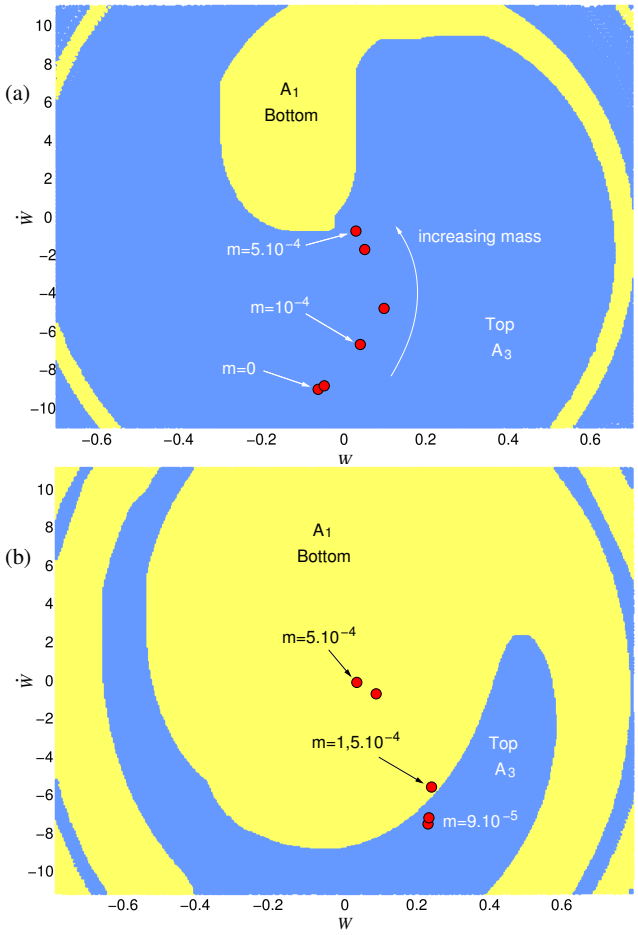

Fig. 5 Basin of attraction of Design 2 without added mass, $V_{dc} = 100V_{ac} = 1.9V$.(a): $\Omega_{op} = 22.3274$; (b): $\Omega_{op} = 22.325$. Basin of attraction of point A_1(yellow) and point A_3 (blue).

mass defines a unique limit cycle, and the moment of its take-off defines a unique point on this limit cycle, and thus unique initial conditions for the escape from A_2. Establishing the basins of attraction of the microbeam without added mass, and identifying these initial conditions for several values of m (indicated by red dots on Fig 5.a), permits to determine which point (A_1 or A_3) is reached. It can be shown that, depending on the moment when the solution escapes the periodic limit cycle, the basin of attraction and the initial conditions simply undergo a rotation and keep the same relative position. In other words, the jump down to A_1 or up to A_3 does not depend on the moment when the mass takes off. From the computations at $\Omega_{op} = 22.3274$, it turns out that for mass ratios $m \leq 5.10^{-4}$, i.e. for values $m_p \leq 10^{-16}kg$, the jump always occurs towards the upper solution A_3 and consequently the bifurcation-based detection does not work anymore (see Fig. 5.a).

In Fig. 5.b, with the forcing frequency $\Omega_{op} = 22.325$, the basin of attraction of the bottom stable solution is larger and A_1 is reached when $m > 1.5 \times 10^{-4}$, i.e. $m_p > 3.10^{-17}kg$. Since the masses of interest are much lower than this value, it can be concluded that the system never returns to its initial stable position, i.e. it is not reinitialized, and thus the bifurcation-based detection only works once.

A reinitialization solution, see Fig. 2, consists in first decreasing the operating frequency Ω_{op} until point B_2 then jumping down to point B_1 and finally increasing the frequency again up to point A_1.

For the hardening behavior, the reinitialization is also presented in Fig. 4. After the take-off of the added mass, the response arrives at A_3 (close to A_2) and it cannot return to A_1, see Fig. 4. Thus the reinitialization is necessary to return to the operating point A_1. Firstly, the frequency is decreased from Ω_{A_3} to Ω_{B_1}. Here, the response jumps to B_2, then the frequency is increased up to the operating frequency Ω_{A_1}.

However, some drawbacks arise: because of the small jump from A_2 to A_3 (Fig. 2 or 4), the "take-off" moment of the added mass is difficult to detect. So the moment when the reinitialization must be performed remains unknown.

3.5 Automatic reinitialization

The aforementioned problems of reinitialization can be overcome by using a slow time-varying frequency sweep such as:

$$\Omega(t) = \Omega_{op} + \delta\cos(\varepsilon\pi t + \phi) \tag{12}$$

with the sweep velocity $\varepsilon << \Omega_{op}$. $\Omega_{max} = \Omega_{op} + \delta$ and $\Omega_{min} = \Omega_{op} - \delta$ are the frequency-sweep boundaries.

In Fig. 6.a, several successive frequency sweep-up and sweep-down according to Eq. (12) are performed and W (respectively Ω) is plotted versus non-dimensional time t (Fig. 6.a, respectively 6.b).

In Fig. 6.a, variations of W versus t permit to distinguish some phases 1-2-3-4-5/1-2-3-4-5/... of the behavior, which are presented in in Fig. 6.c as a frequency-amplitude plot. This sequence of phases defines the hysteretic cycle obtained by a dynamical variation of Ω: in the limit case of quasi-static evolution of Ω ($\varepsilon \to 0^+$), the hysteretic cycle corresponding to the theoretical response curve of Fig. 2 with added mass is obtained.

3.5.1 Frequency-sweep principle for the softening behavior

This subsection presents the principle of the frequency sweep for the softening behavior. It is illustrated with theoretical response curves determined by the Asymptotic Numerical Method.

The frequency sweep $\Omega(t)$ is illustrated in Fig. 7. Ω^0_{bif1} and Ω^0_{bif2} are the two bifurcation frequencies of the response without added mass and the maximum and minimum frequencies Ω_{min} and Ω_{max} are set below Ω^0_{bif1} and Ω^0_{bif2} respectively. $\Delta\Omega = \Omega^0_{bif1} - \Omega_{min}$ defines the frequency shift

Produit par HAL - 16 Sep 2014

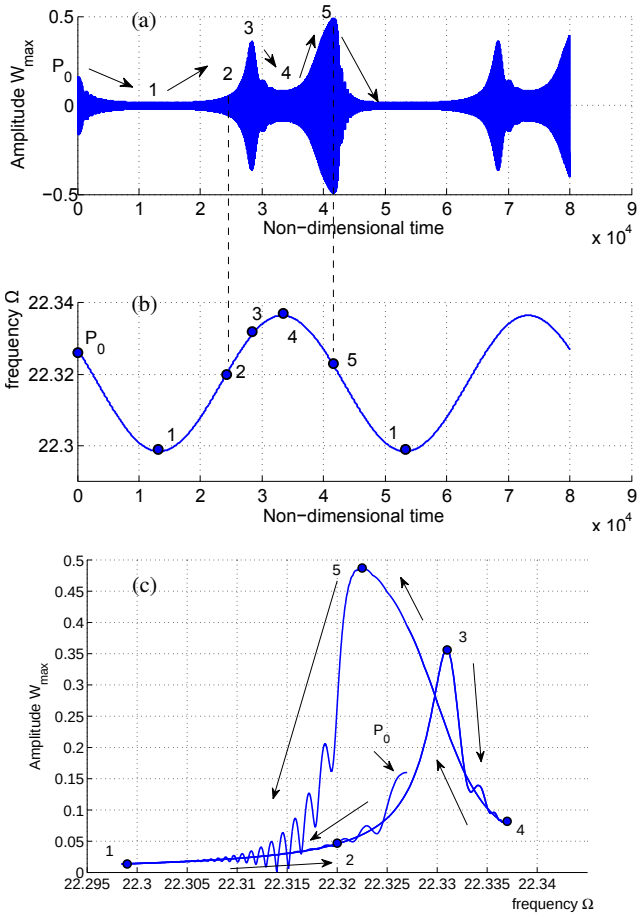

Fig. 6 Determination of the frequency-sweep response. (a) amplitude $W(t)$; (b) frequency $\Omega(t)$; (c) frequency-sweep response.

of the maximal added mass to be detected. $\Omega^0_{bif1} - \Omega_{max} = \Delta\Omega - 2\delta$ defines the threshold of mass detection.

Fig. 7 illustrates specifically the cycle without added mass. The response follows the curve between points A and B. There is no hysteretic cycle nor associated amplitude jump.

The detection of a mass variation, for instance a bioparticle falling on the microbeam, is illustrated in Fig. 8 where the frequency sweep defines hysteretic cycles corresponding to the two following cases:

- In the first case, shown in Fig. 8.a, the particle falls at the moment (point 1) when the sweep frequency Ω remains lower than Ω^m_{bif1}. So the response goes through the hysteretic cycle according to the path joined by the succession of the following points: 1-2/3-4-5-6-7-8/3-4-5-6-7-8/..., there are amplitude jumps from 3 to 4 and from 6 to 7 in a cyclic manner.
- In the second case, shown in Fig. 8.b, the particle falls at the moment (point 1) when the sweep frequency is between Ω^m_{bif1} and Ω^0_{bif}. The response path is: 1-2/3-4-5-6-7-8/3-4-5-6-7-8/... When the particle falls on the beam, the amplitude first jumps from 1 to 2. Then there are two amplitude jumps from 7 to 8 and from 4 to 5 in a cyclic manner.

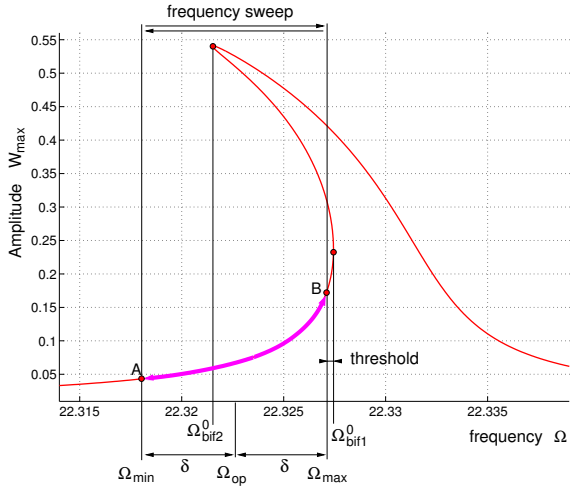

Fig. 7 Principle of frequency sweep without added mass. The response goes back-and-forth between points A and B.

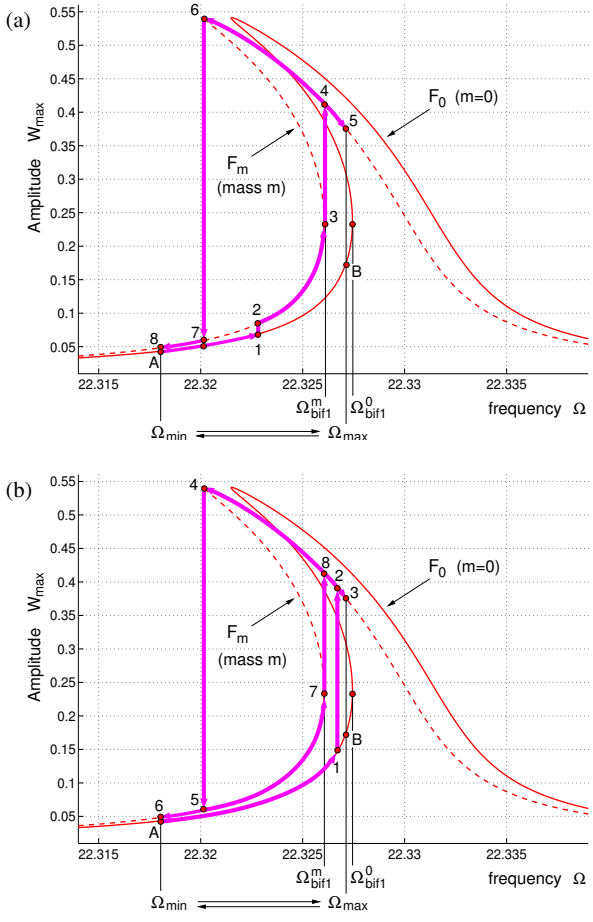

Fig. 8 Responses with added mass. An added mass arrives when $\Omega < \Omega^m_{bif1}$ (a) or when $\Omega \geq \Omega^m_{bif1}$ (b). The response follows hysteretic cycles.

Produit par HAL - 16 Sep 2014

Produit par HAL - 16 Sep 2014

When the particle takes off, the response is presented in Fig. 9. The two following cases are distinguished:

- In the first case, shown in Fig. 9.a, the particle takes off at the moment when the sweep frequency is lower than Ω^0_{bif2}. The starting point is 1 or 1' depending on whether the response starts from the top or the bottom of the curve F_M and the response path is then: 1 or 1'-2/A-B/A-B/... After a jump to point 2, the response follows the curve F_0 between points A and B, i.e. the response curve without added mass of Fig. 7. There is no hysteretic cycle nor amplitude jump.
- In the second case, shown in Fig. 9.b, the particle takes off at the moment when the sweep frequency is higher than Ω^0_{bif2}: the starting point is 1 or 1' and the response jumps to top point 2' or bottom point 2. If there is a jump down to 2, the response path is then: 1 or 1'-2/B-A/B-A/... After a jump to point 2, the response is the part of the curve F_0 between points A and B. If there is a jump up to 2', the response path is then: 1 or 1'-2'-3'-4'-4/A-B/A-B/... After two successive jumps up to 2' and down to 4, the response also goes back-and-forth between A and B as in Fig. 7.

Hence when varying the frequency from Ω_{min} up to Ω_{max}, the steady response path presents a maximum of amplitude $W_{max} > 0.5$ with added mass (Fig. 8), whereas $W_{max} < 0.2$ without added mass(Fig. 7). The detection principle is based on this difference.

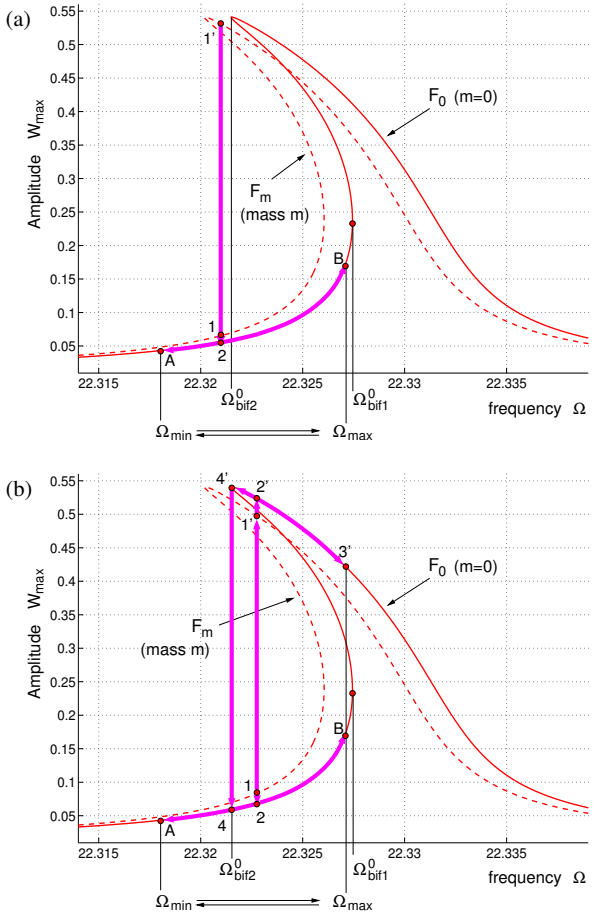

Fig. 9 Responses after mass take-off triggered when $\Omega < \Omega^0_{bif2}$ (a) or when $\Omega \geq \Omega^m_{bif1}$ (b).

3.5.2 Numerical example of the frequency sweep for the softening behavior

In order to validate the frequency-sweep principle presented in subsection 3.5.1, a numerical example with a given ε is presented in what follows.

Let us consider Design 2 and the following frequency sweep:

$$\Omega(t) = 22.317 + 0.01\sin(10^{-5}\pi t), \tag{13}$$

corresponding to the physical values:

$$\tilde{\Omega}(\tilde{t}) = 8.1866\times10^6 + 3.67\times10^3\sin(23\pi\tilde{t})\,(Hz). \tag{14}$$

Let the added mass remain on the beam during two sweep periods in such a way that no additional added mass falls on the beam in the mean time.

Fig. 10.a shows the evolution of W_{max} versus time for several periods of the frequency sweep. The following scenario is considered: from an initial position P_0, the micro-beam vibrates without added mass. The steady-state regime is reached after transient regime from P_0 to P_1 (see Fig. 10.b). Then, at point 1, the added mass m_1 falls on the micro-beam (dashed line) and the response path is 1/2-3-4-5-6/2-3-4-5-6... After two sweep periods, this added mass leaves the micro-beam at point 7 and the beam continues to vibrate without added mass. Finally, the process is iterated from point 8, with another mass m_2.

In Fig. 10.a, the time history response shows that in the presence of the added mass on the beam, the peaks are larger than 0.5 for two successive periods. Hence, for the softening behavior, the detection principle is based on amplitude jumps and on the change of maximum amplitude.

In Fig. 10.b, the transient regime and the corresponding steady-state response curve are plotted, providing the hysteretic cycle described by the sequence of numbered points. This curve is used again in the next section to quantify the added mass.

3.5.3 Frequency-sweep principle for the hardening behavior

Similarly to subsection 3.5.1, the frequency-sweep principle is illustrated with the theoretical response determined by the ANM.

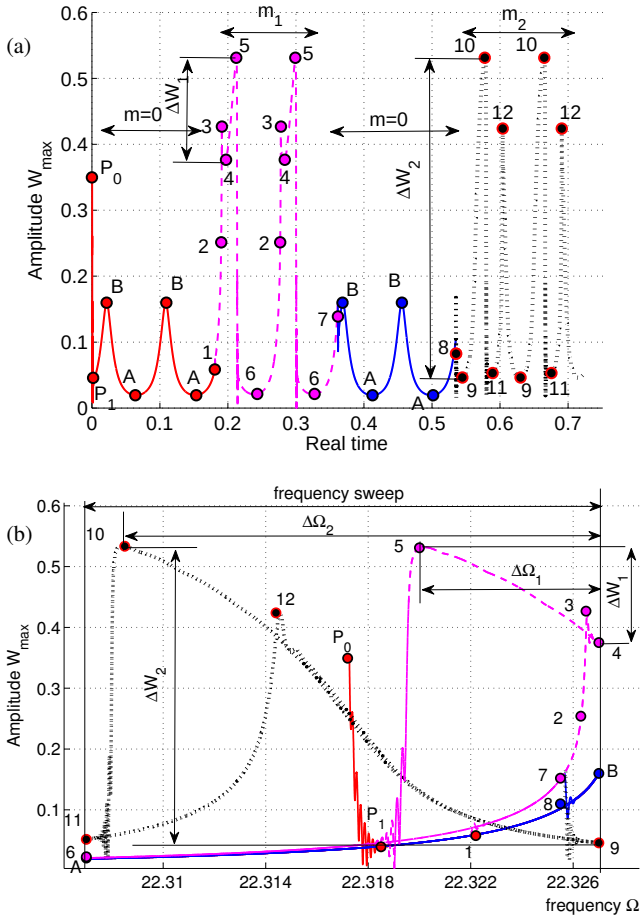

Fig. 10 Frequency sweep for Design 2. (a): response $W_{max} - t$; (b): response $W_{max} - \Omega$. Without added mass (solid line); with small added mass (dashed line) and big added mass (dotted line).

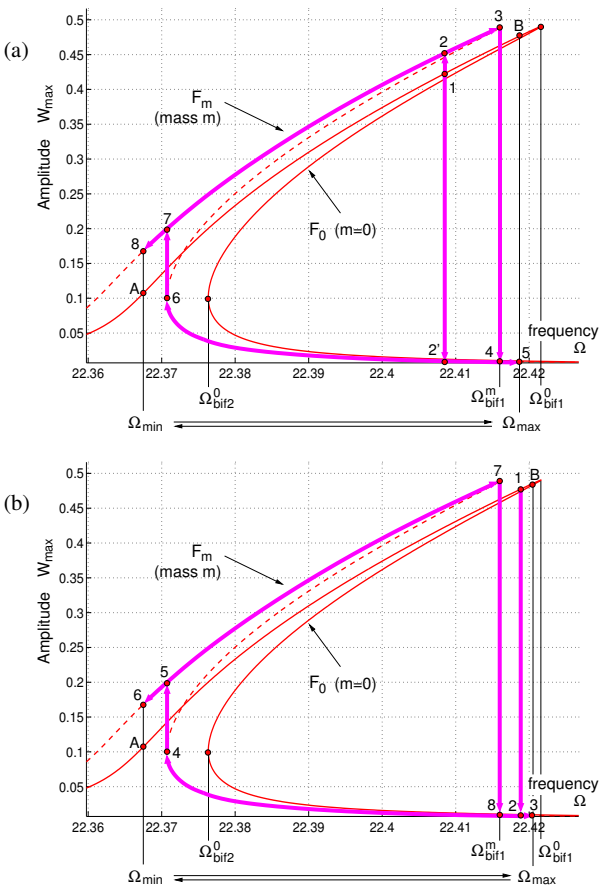

Fig. 11 Responses with an added mass arriving when $\Omega < \Omega^m_{bif1}$ (a) or when $\Omega \geq \Omega^m_{bif1}$ (b).

The frequency varies slowly according to (12), with $\Omega_{min} < \Omega^0_{bif2}$ and $\Omega_{max} < \Omega^0_{bif1}$. Without added mass, the steady response is $A - B/A - B/\ldots$. When the particle falls on the beam, the two following cases are distinguished:

– In the first case, shown in Fig. 11.a, the particle arrives when the sweep frequency is lower than Ω^m_{bif1}. The response path is 1-2/3-4-5-6-7-8/3-4-5-6-7-8/... or 1-2'/4-5-6-7-8-3/4-5-6-7-8-3/...
– In the second case, shown in Fig. 11.b, the particle arrives when the sweep frequency is larger than Ω^m_{bif1}. The response curve is 1-2/3-4-5-6-7-8/3-4-5-6-7-8/...

So the response with added mass is the hysteretic cycle with two amplitude jumps at the bifurcation frequencies.

When the added mass takes off, the two following cases are distinguished:

– In the first case, shown in Fig. 12.a, the added mass takes off at the moment when the sweep frequency is lower than Ω^0_{bif2}. The starting point is 1 or 1' and the response path is then: 1 or 1'-2/A-B/A-B/...
– In the second case, shown in Fig. 12.b, the added mass takes off at the moment when the sweep frequency is larger than Ω^0_{bif2}. The starting point is 1 or 1'. If jumping to 2, the response path is then: 1 or 1'-2/3-4-4'/A-B/A-B/... If jumping to 2', the response path is then: 1 or 1'-2'/B-A/B-A/...

Hence when sweeping from Ω_{min} to Ω_{max}, the steady-state response without added mass is the branch $A - B$, with no hysteretic cycle. So there is no amplitude jump and the minimum amplitude is obtained at point A ($W_{max}(A)$). The steady-state response with added mass follows the hysteretic cycle of Fig. 11, with two amplitude jumps. The minimum amplitude is very small. Its measurement could be difficult in the presence of noise.

3.5.4 Numerical example of the frequency sweep for the hardening behavior

Let us consider the following frequency sweep for Design 1 exhibiting the hardening behavior:

$$\Omega(t) = 22.3956 + 0.0256\sin(5.10^{-5}\pi t), \qquad (15)$$

Produit par HAL - 16 Sep 2014

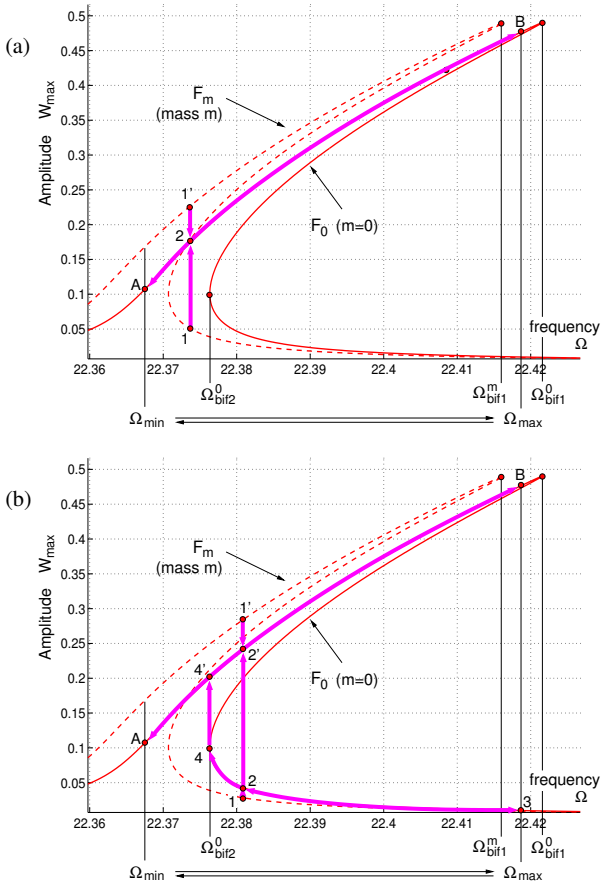

Fig. 12 Responses after mass take-off triggered when $\Omega < \Omega^0_{bif2}$ (a) or when $\Omega \geq \Omega^m_{bif1}$ (b).

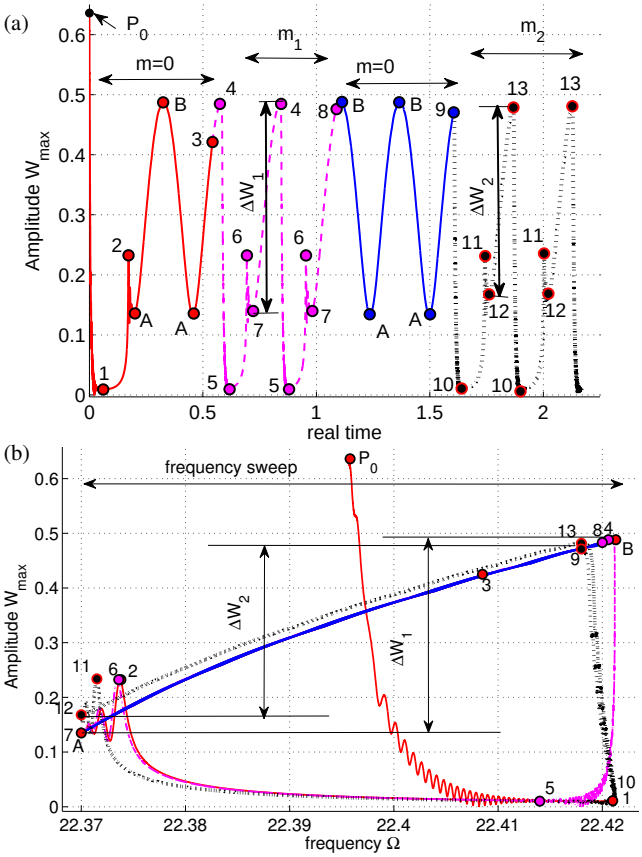

Fig. 13 Frequency sweep for Design 1: without added mass (solid line), with small mass $m_1 = 10^{-5}$ (dashed line) and bigger mass $m_2 = 10^{-4}$ (dotted line). (a): response $W_{max} - t$; (b): response $W_{max} - \Omega$.

corresponding to the physical values:

$$\tilde{\Omega}(\tilde{t}) = 5.477 \times 10^5 + 620\sin(7.68\pi\tilde{t})\,(Hz). \qquad (16)$$

In Fig. 13.a, without added mass, the response (solid line) does not show any amplitude jump. Once the steady-state regime has been reached, the response is the branch $A-B$, see Fig. 13.b with a change in amplitude from $W_{max} = 0.49$ at point B to $W_{max} = 0.14$ at point A. At moment 3, an added mass $m_1 = 10^{-5}$ falls on the beam. The response (dashed line) jumps from a maximum amplitude $W_{max} \simeq 0.49$ (point 4) to a minimum amplitude $W_{max} \simeq 0.01$ (point 5). After two sweep periods, the added mass takes off at point 8, the response goes back to the branch $A-B$ with no jump. At point 9, an another mass $m_2 = 10^{-4}$ arrives, and the response jumps from a maximum amplitude $W_{max} \simeq 0.49$ (point 13) to a minimum amplitude $W_{max} \simeq 0.01$ (point 10).

Hence, for the hardening behavior, the detection principle is based on amplitude jumps and on the change of minimum amplitude.

From a theoretical point of view, there is no real advantage in using either softening or hardening behavior for mass detection. The respective hysteretic cycles are basically reversed, with similar properties. As shown in Figs. 10.a and 13.a, an event is characterized by a clear change in the maximum/minimum amplitude in the case of softening/hardening behavior respectively, and by large jumps in both cases.

3.6 Mass-detection threshold

Theoretically, if it is possible to set exactly $\Omega_{max} = \Omega^0_{bif1}$, then any mass without any lower limit will cause a jump in amplitude. However, in practice, this is either not possible because of the limited resolution of the instrumentation or not desirable in order to avoid unwanted jumps due to noise-related perturbations. As a consequence, Ω_{max} is set such that $\Omega_{max} < \Omega^0_{bif1}$, and the difference between Ω_{max} and Ω^0_{bif1} governs the threshold providing the minimal mass that can be detected.

For example, in Fig. 14, at $\Omega_{op} = 22.325$, a large jump from P_0 ($W_{max} = 0.09$) to P_2 on the dotted line ($W_{max} = 0.42$) indicates the presence of masses $m \geq 9.10^{-5}$. For masses

Produit par HAL - 16 Sep 2014

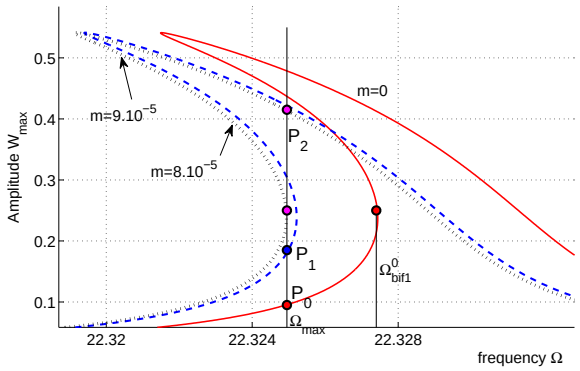

Fig. 14 Detection threshold of Design 2 at $\Omega_{op} = 22.325$ and $V_{dc} = 10V_{ac} = 9V$, without added mass (solid line), $m = 8 \times 10^{-5}$ (dashed line), $m = 9 \times 10^{-5}$ (dotted line).

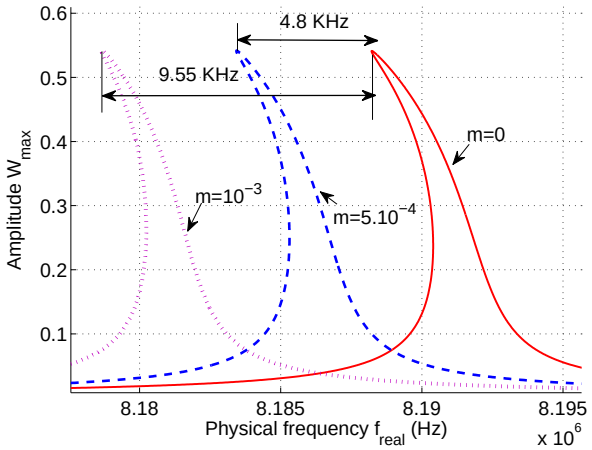

Fig. 15 Design 2: quantification with frequency shift, for $V_{dc} = 100V_{ac} = 1.9V$, without added mass (solid line), $m = 5.10^{-4}$(dashed line); $m = 10^{-3}$(dotted line).

$m < 9.10^{-5}$, for instance $m = 8.10^{-5}$, there is only a small jump from P_0 to P_1 instead of the upper point near P_2, as confirmed by a study of the basin of attraction.

4 Quantification of an added mass

4.1 Quantification via frequency shift

Let x_0 be the position of the added mass on the beam. If $\phi(x_0) \neq 0$, there is always a frequency shift of the response curve depending on the added mass. Hence, the frequency shift $\Delta\Omega$ is measured to identify the mass (see Fig. 15). Though it is commonly used in the linear regime, this type of quantification is even more interesting in the nonlinear regime since W_{max} is larger and easier to discriminate from the measurement noise. However, in both cases, the relation between $\Delta\Omega$ and the added mass m is linear, thus the quantification becomes all the more difficult as the mass decreases.

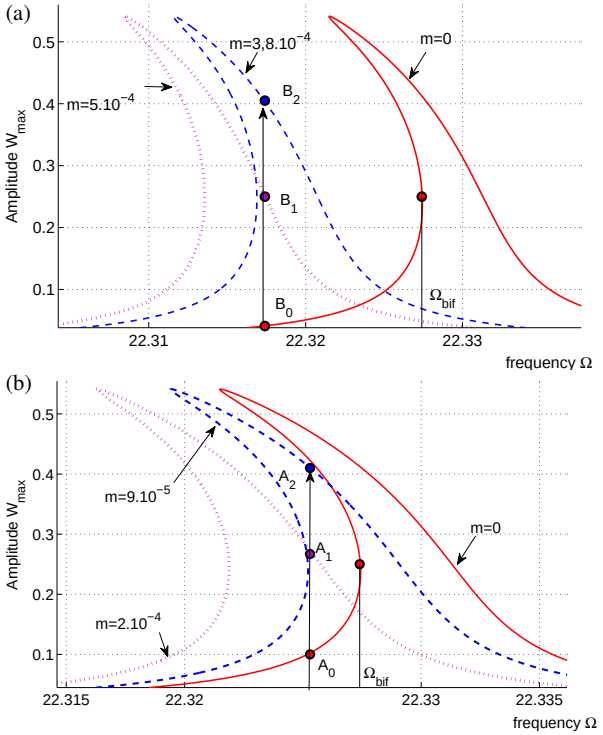

Fig. 16 Design 2: quantification with amplitude jumps at two fixed frequencies. (a): $\Omega = 22.317$; (b): $\Omega = 22.325$.

4.2 Quantification via amplitude jumps

4.2.1 Using fixed frequency

For the hardening behavior, with a large or small added mass, there is always a jump from a large value to a small value of W_{max}, see Fig. 11 and 13. The detection of the added mass is possible but its quantification is difficult with a fixed frequency Ω_{op} since the amplitude of the jump is almost the same whatever the value of the added mass.

For the softening behavior, at a fixed frequency Ω_{op}, the amplitude of the jump depends on the value of the mass: a small mass induces a large jump and vice versa. Using only one fixed frequency is not sufficient to quantify a large range of added masses. Using several fixed frequencies changes the threshold of detection (see section 3.6) and permits to improve this range of quantifiable masses or to set the upper and lower bounds of masses to be detected.

In Fig. 16, at $\Omega_{op} = 22.317$, the masses $3.8 \times 10^{-4} \leq m \leq 5.10^{-4}$ are quantified by jumps from $W_{max} = 0.02$ to $W_{max} = 0.25$ or 0.4. When Ω_{op} approaches Ω_{bif} more closely, i.e. $\Omega_{op} = 22.325$, masses $9.10^{-5} \leq m \leq 2.10^{-4}$ are quantified by the jumps from 0.1 to 0.25 or 0.4.

Produit par HAL - 16 Sep 2014

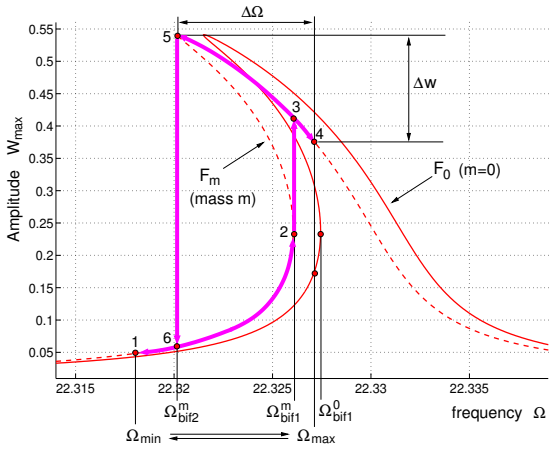

Fig. 17 Quantification via frequency sweep for design 2 (softening behavior).

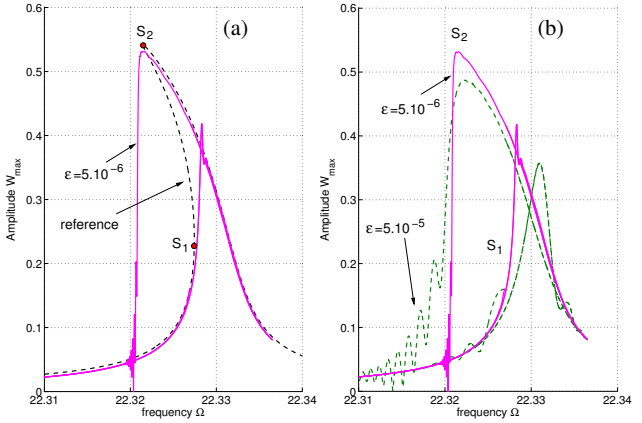

Fig. 18 Influence of ε on the response. (a) for $\varepsilon = 5.10^{-6}$ (solid line) and reference response with ANM (dashed-dotted line); (b) $\varepsilon = 5.10^{-6}$ (solid line) and $\varepsilon = 5.10^{-5}$ (dashed line).

4.2.2 Quantification via frequency sweep and hysteretic cycles

In the case with added mass, for the softening behavior (respectively for the hardening behavior), ΔW and $\Delta\Omega$ are the amplitude and frequency differences between two points, one point having the maximal amplitude, another the maximal frequency Ω_{max} (respectively the minimal frequency), as represented in Fig. 17.

Similarly to subsections 3.5.2 and 3.5.4, the frequency sweep can be used to quantify the added mass. In Fig. 10.b, the quantification can be carried out using the values ΔW_1, ΔW_2 or $\Delta\Omega_1$, $\Delta\Omega_2$. So in comparison with quantification at fixed frequency, the frequency sweep is more interesting: the added mass can fall at any moment and the quantification is automatic.

However, for the frequency sweep, the accuracy of the quantification depends on the non-dimensional sweep velocity ε of Eq. (12). Since the frequency sweep is essentially transient, numerical results are computed by means of a time integration scheme (Runge-Kutta). Two cases of frequency sweep with different sweep velocity ε are compared with the reference steady-state response curve obtained with the ANM. In Fig. 18.a, the response curve for $\varepsilon = 5.10^{-6}$ and the ANM are similar. However for a large ε ($\varepsilon = 5.10^{-5}$), the response is strongly modulated (see Fig. 18.b). The jumps are not vertical and do not coincide precisely with the bifurcation position S_1 and S_2. Choosing a small ε is therefore required but ε also decides the quantification time. If ε is too small, the quantification time is very long, thus there is a risk that the added mass takes off before the quantification end.

5 Localization of an added mass

For a clamped-clamped microbeam, the frequency shift is determined by (see Appendix):

$$\Delta_{f_i} = \frac{\omega_i - \omega_{i0}}{\omega_{i0}} \approx -\frac{1}{2} m \phi_i^2(x_0), \tag{17}$$

with x_0 the position of the added mass, ω_{i0} and ω_i the resonant frequencies of the i^{th} mode without and with the added mass respectively. There are one equation and two unknowns, thus the resonance at the frequency of another mode has to be considered. Due to the symmetry of the clamped-clamped beam let the first and third mode shapes be selected. Considering the resonance at the frequencies of the first and third modes permits to determine x_0 and m:

$$\begin{cases} \Delta_{f1} \approx -\frac{1}{2} m \phi_1^2(x_0),\ \Delta_{f3} \approx -\frac{1}{2} m \phi_3^2(x_0), \\ \left(\frac{\phi_3(x_0)}{\phi_1(x_0)}\right)^2 = \frac{\Delta_{f3}}{\Delta_{f1}}. \end{cases} \tag{18}$$

The principle of localization is illustrated in Fig. 19. First, the frequency shifts Δ_{f1} and Δ_{f3} between curves with and without added mass are determined at the resonant frequency of the first and third modes. Then, the position of the added mass is located from the ratio $\sqrt{\Delta_{f3}/\Delta_{f1}}$.

For example, let us consider design 1 (hardening behavior) with $V_{dc1} = 10V_{ac1} = 9V$ at the resonant frequency of the first mode and $V_{ac2} = 1.5V_{dc2} = 67.5V$ for the third mode. Several arbitrary values for m_0, x_0 are first used to generate the responses with added mass. Then, the principle of localization is used to identify the values of m_0, x_0 from the knowledge of these curves only. To this end, Δ_{f1} and Δ_{f3} are measured on the responses and two couples of solutions (m_1, x_1), (m_2, x_2) are calculated from the system (18). Incorrect values (m_2, x_2) can be eliminated by considering the resonance at the frequency of the higher-mode. Table 3 shows

Produit par HAL - 16 Sep 2014

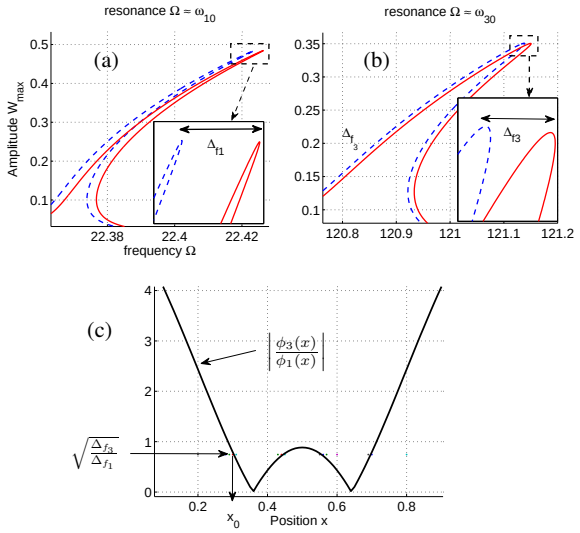

Fig. 19 Principle of localization. Frequency shift at the (a) first and (b) third mode; without added mass(solid line), with added mass (dashed line). Ratio of the third and first mode shapes along the beam axis (c).

$m_0.10^{-4}$	x_0	$\Delta_{f1}.10^4$	$\Delta_{f3}.10^4$	$\lvert\phi_3/\phi_1\rvert$
5	0.5	6.089	4.987	0.9051
1	0.5	1.2182	0.997	0.904
1	0.35	0.86	0.0132	0.1239
1	0.2	0.185	1.141	2.484
0.5	0.2	0.0928	0.574	2.488
10	0.1	0.133	3.101	4.823

$m_1.10^{-4}$	x_1	$m_2.10^{-4}$	x_2	$\frac{x_1-x_0}{x_0}$	$\frac{m_1-m_0}{m_0}$
4.83	0.5	10	0.2926	exact	3.4 %
0.96	0.5	2.15	0.2926	exact	4%
1.03	0.348	0.92	0.3697	0.5%	3 %
1.009	0.197	-	-	1.45%	0.9%
0.5078	0.1969	-	-	1.55%	1.56 %
0.0125	0.0472	-	-	large	large

Table 3 Design 1: example of localization. At $\Omega \approx \omega_{10}$, $V_{dc} = 10V_{ac} = 9V$; at $\Omega \approx \omega_{30}$, $V_{ac} = 1.5V_{dc} = 67.5V$.

that the localization is exact for positions close to the middle of the beam. For positions close to the ends of the beam, the deviation is large because $\phi_k(x_0)$ is small at these positions, yielding a small frequency shift.

This procedure only depends on the experimental measure of Δ_{f1} and Δ_{f3} and is therefore identical for both softening and hardening behaviors.

6 Conclusion

An alternative mass sensing technique based on nonlinear micro/nanoelectromechanical resonant sensors has been numerically investigated. The detection takes advantage of bistability and bifurcations of the hysteretic nonlinear responses of the electrostatically-actuated resonator. Contrary to the classical detection based on the frequency shift induced by an additional mass, sudden jumps in amplitude make the detection of a very small mass possible. Another interesting feature lies in the fact that the limit of detection can be set with the value of the operating frequency. However, when operating at fixed frequency, it appears that this bifurcation-based mass detection does not exhibit the expected robustness. A possible improvement has been proposed, based on a frequency sweep which varies slowly in sinusoidal form around the resonance and automatically forces the reinitialization of the detection, thus enabling real-time ultrasensitive detection and quantification. The localization of an added mass is very satisfactory for positions far enough from clamped ends of the sensor. This bifurcation-based mass detection will be investigated experimentally in a near future in order to validate the numerical results presented in this paper. This single sensing device is a first step towards the use of NEMS arrays [38]. In the long term, it could lead to new mass measurement architectures and open prospect to miniaturized mass spectrometers with very high analysis rate. In this perspective, robustness to noise of the proposed bifurcation-based sensing technique will be of prime interest. Some works address the problem of noise sensitivity of the systems when one adds a small mass and consider noise-induced switching near bifurcation points [32] [39,40] [41, 42] [43] [44]. These developments will be needed but are beyond the goal of this paper.

Acknowledgements The authors are indebted to the institute Carnot Ingénierie@Lyon (I@L) for its support and funding.

References

1. B. Ilic, Y. Yang, H. Craighead, Virus detection using nanoelectromechanical devices, Appl. Phys. Lett. **85**(13), 2604–2606 (2004). DOI 10.1063/1.1794378
2. S. Velanki, H.F. Ji, Detection of feline coronavirus using microcantilever sensors, Meas. Sci. Technol. **17**(11), 2964–2968 (2006). DOI 10.1088/0957-0233/17/11/015
3. K. Buchapudi, X. Huang, X. Yang, H. Ji, T. Thundat, Microcantilever biosensors for chemicals and bioorganisms, Analyst **136**, 1539–1556 (2011). DOI 10.1039/C0AN01007C
4. J. Gimzewski, C. Gerber, E. Meyer, R. Schlittler, Observation of a chemical reaction using a micromechanical sensor, Chem. Phys. Lett. **217**(5-6), 589–594 (1994). DOI 10.1016/0009-2614(93)E1419-H
5. T. Thundat, E. Wachter, S. Sharp, R. Warmack, Detection of mercury vapor using resonating microcantilevers, Appl. Phys. Lett. **66**(13), 1695–1697 (1995). DOI 10.1063/1.113896
6. E.A. Wachter, T. Thundat, Micromechanical sensors for chemical and physical measurements, Rev. Sci. Instrum. **66**(6), 3662–3667 (1995). DOI 10.1063/1.1145484
7. P. Datskos, S. Rajic, M. Sepaniak, N. Lavrik, C. Tipple, L. Senesac, I. Datskou, Chemical detection based on adsorption-induced and photoinduced stresses in microelectromechanical systems devices, J. Vac. Sci. Technol. B **19**(4), 1173–1179 (2001). DOI 10.1116/1.1387082
8. A. Nayfeh, H. Ouakad, F. Najar, S. Choura, E. Abdel-Rahman, Nonlinear dynamics of a resonant gas sensor, Nonlinear Dyn. **59**(4), 607–618 (2010). DOI 10.1007/s11071-009-9567-z

Produit par HAL - 16 Sep 2014

Produit par HAL - 16 Sep 2014

9. K. Turner, C. Burgner, Z. Yie, E. Holtoff, Using nonlinearity to enhance micro/nanosensor performance, in *Sensors, 2012 IEEE*. pp. 1–4 (2012). DOI 10.1109/ICSENS.2012.6411564
10. N. Kacem, S. Hentz, S. Baguet, R. Dufour, Forced large amplitude periodic vibrations of non-linear mathieu resonators for microgyroscope applications, Int. J. Non Linear Mech. **46**(10), 1347–1355 (2011). DOI 10.1016/j.ijnonlinmec.2011.07.008
11. J. Chaste, A. Eichler, J. Moser, G. Ceballos, R. Rurali, A. Bachtold, A nanomechanical mass sensor with yoctogram resolution, Nat. Nanotechnol. **7**(5), 301–304 (2012). DOI 10.1038/nnano.2012.42
12. B. Ilic, H. Craighead, S. Krylov, W. Senaratne, C. Ober, P. Neuzil, Attogram detection using nanoelectromechanical oscillators, J. Appl. Phys. **95**(7), 3694–3703 (2004). DOI 10.1063/1.1650542
13. M. Hanay, S. Kelber, A. Naik, D. Chi, S. Hentz, E. Bullard, E. Colinet, L. Duraffourg, M. Roukes, Single-protein nanomechanical mass spectrometry in real time, Nat. Nanotechnol. **7**, 602–608 (2012). DOI 10.1038/NNANO.2012.119
14. K. Ekinci, X. Huang, M. Roukes, Ultrasensitive nanoelectromechanical mass detection, Appl. Phys. Lett. **84**(22), 4469–4471 (2004). DOI 10.1063/1.1755417
15. E. Buks, B. Yurke, Mass detection with a nonlinear nanomechanical resonator, Phys. Rev. E **74**, 046,619 (2006). DOI 10.1103/PhysRevE.74.046619
16. N. Kacem, S. Baguet, S. Hentz, R. Dufour, Nonlinear phenomena in nanomechanical resonators: mechanical behaviors and physical limitations, Mech. Ind. **11**(6), 521–529 (2010). DOI 10.1051/meca/2010068
17. W. Xie, H. Lee, S. Lim, Nonlinear dynamic analysis of mems switches by nonlinear modal analysis, Nonlinear Dyn. **31**(3), 243–256 (2003). DOI 10.1023/A:1022914020076
18. A. Nayfeh, M. Younis, E. Abdel-Rahman, Dynamic pull-in phenomenon in mems resonators, Nonlinear Dyn. **48**(1-2), 153–163 (2007). DOI 10.1007/s11071-006-9079-z
19. N. Kacem, S. Baguet, S. Hentz, R. Dufour, Pull-in retarding in nonlinear nanoelectromechanical resonators under superharmonic excitation, J. Comput. Nonlinear Dyn. **7**(2), 021,011–021,011 (2012). DOI 10.1115/1.4005435
20. M. Narducci, E. Figueras, M. Lopez, I. Gracia, J. Santander, P. Ivanov, L. Fonseca, C. Cané, Sensitivity improvement of a microcantilever based mass sensor, Microelectron. Eng. **86**(4-6), 1187–1189 (2009). DOI 10.1016/j.mee.2009.01.022
21. S. Dohn, R. Sandberg, W. Svendsen, A. Boisen, Enhanced functionality of cantilever based mass sensors using higher modes and functionalized particles, in *The 13th International Conference on Solid-State Sensors, Actuators and Microsystems. TRANSDUCERS '05.*, vol. 1. vol. 1, pp. 636 – 639 (2005). DOI 10.1109/SENSOR.2005.1496497
22. H. Xie, J. Vitard, S. Haliyo, S. Régnier, Enhanced sensitivity of mass detection using the first torsional mode of microcantilevers, Meas. Sci. Technol. **19**(5), 055,207 (2008). DOI 10.1088/0957-0233/19/5/055207
23. N. Lobontiu, I. Lupea, R. Ilic, H. Craighead, Modeling, design, and characterization of multisegment cantilevers for resonant mass detection, J. Appl. Phys. **103**(6), 064,306 (2008). DOI 10.1063/1.2894900
24. R. Dufour, A. Berlioz, Parametric instability of a beam due to axial excitations and to boundary conditions, J. Vib. Acoust. **120**(2), 461–467 (1998)
25. W. Zhang, R. Baskaran, K. Turner, Effect of cubic nonlinearity on auto-parametrically amplified resonant mems mass sensor, Sens. Actuators, A **102**(1), 139–150 (2002). DOI doi:10.1016/S0924-4247(02)00299-6
26. W. Zhang, K. Turner, Application of parametric resonance amplification in a single-crystal silicon micro-oscillator based mass sensor, Sens. Actuators, A **122**(1), 23–30 (2005). DOI 10.1016/j.sna.2004.12.033
27. O. Thomas, F. Mathieu, W. Mansfield, C. Huang, S. Trolier-McKinstry, L. Nicu, Efficient parametric amplification in micro-resonators with integrated piezoelectric actuation and sensing capabilities, Appl. Phys. Lett. **102**(16), 163504 (2013). DOI 10.1063/1.4802786
28. M. Khater, E. Abdel-Rahman, A. Nayfeh, A mass sensing technique for electrostatically-actuated mems, in *ASME DETC 3rd International conference on micro- and nanosystems*, vol. 6. San Diego, USA, vol. 6, pp. 655–661 (2009). DOI 10.1115/DETC2009-87551
29. M. Younis, F. Alsaleem, Exploration of new concepts for mass detection in electrostatically-actuated structures based on nonlinear phenomena, J. Comput. Nonlinear Dyn. **4**(2), 021,010 (2009). DOI 10.1115/1.3079785
30. V. Kumar, J.W. Boley, Y. Yang, H. Ekowaluyo, J.K. Miller, G.T.C. Chiu, J.F. Rhoads, Bifurcation-based mass sensing using piezoelectrically-actuated microcantilevers, Appl. Phys. Lett. **98**(15), 153,510 (2011). DOI 10.1063/1.3574920
31. V. Kumar, Y. Yang, J. Boley, G.C. Chiu, J. Rhoads, Modeling, analysis, and experimental validation of a bifurcation-based microsensor, J. Microelectromech. Syst. **21**(3), 549–558 (2012). DOI 10.1109/JMEMS.2011.2182502
32. R. Harne, K. Wang, A bifurcation-based coupled linear-bistable system for microscale mass sensing, J. Sound Vib. **333**(8), 2241–2252 (2014). DOI 10.1016/j.jsv.2013.12.017
33. C. Guo, G.K. Fedder, Bi-state control of parametric resonance, Appl. Phys. Lett. **103**(18), 183,512 (2013). DOI 10.1063/1.4828564
34. A. Nayfeh, M. Younis, E. Abdel-Rahman, Reduced-order models for mems applications, Nonlinear Dyn. **41**(1-3), 211–236 (2005). DOI 10.1007/s11071-005-2809-9
35. N. Kacem, S. Baguet, S. Hentz, R. Dufour, Computational and quasi-analytical models for non-linear vibrations of resonant mems and nems sensors, Int. J. Non Linear Mech. **46**(3), 532–542 (2011). DOI 10.1016/j.ijnonlinmec.2010.12.012
36. N. Kacem, Nonlinear dynamics of m&nems resonant sensors: design strategies for performance enhancement. Ph.D. thesis, INSA Lyon (2010)
37. B. Cochelin, C. Vergez, A high order purely frequency-based harmonic balance formulation for continuation of periodic solutions, J. Sound Vib. **324**(1-2), 243–262 (2009). DOI 10.1016/j.jsv.2009.01.054
38. S. Gutschmidt, O. Gottlieb, Nonlinear dynamic behavior of a microbeam array subject to parametric actuation at low, medium and large dc-voltages, Nonlinear Dyn. **67**(1), 1–36 (2012). DOI 10.1007/s11071-010-9888-y
39. C. Stambaugh, H. Chan, Noise-activated switching in a driven nonlinear micromechanical oscillator, Phys. Rev. B **73**, 172,302 (2006). DOI 10.1103/PhysRevB.73.172302
40. H.B. Chan, C. Stambaugh, Activation barrier scaling and crossover for noise-induced switching in micromechanical parametric oscillators, Phys. Rev. Lett. **99**, 060,601 (2007). DOI 10.1103/PhysRevLett.99.060601
41. M.I. Dykman, M. Khasin, J. Portman, S.W. Shaw, Spectrum of an oscillator with jumping frequency and the interference of partial susceptibilities, Phys. Rev. Lett. **105**, 230,601 (2010). DOI 10.1103/PhysRevLett.105.230601
42. N. Miller, C. Burgner, M. Dykman, S. Shaw, K. Turner, Fast estimation of bifurcation conditions using noisy response data, in *Proc. SPIE 7647, Sensors and Smart Structures Technologies for Civil, Mechanical, and Aerospace Systems*. p. 76470O (2010). DOI 10.1117/12.847585
43. M. Requa, K. Turner, Precise frequency estimation in a microelectromechanical parametric resonator, Appl. Phys. Lett. **90**(17), 173,508 (2007). DOI 10.1063/1.2732172
44. Z. Yie, M. Zielke, C. Burgner, K. Turner, Comparison of parametric and linear mass detection in the presence of detection

noise, J. Micromech. Microeng. **21**(2), 025,027 (2011). DOI 10.1088/0960-1317/21/2/025027

Appendix

Let m_p and x_0 be the physical mass and position of the added mass, and ω_i^m, $\phi_i^m(x)$ and $\omega_i^0, \phi_i^0(x)$ the frequencies and eigenmodes corresponding to cases with and without added mass. The equation of motion for an infinitesimal volume $d\tilde{x}$ without excitation and damping force is:

$$\frac{\partial}{\partial \tilde{x}^2}\left(EI\frac{\partial^2 \tilde{w}}{\partial \tilde{x}^2}\right)\mathrm{d}\tilde{x} + \rho S\frac{\partial^2 \tilde{w}}{\partial \tilde{t}^2}\mathrm{d}\tilde{x} + m_p\delta_{\tilde{x}_0}(\tilde{x})\frac{\partial^2 \tilde{w}}{\partial \tilde{x}^2} = 0 \tag{19}$$

Using the nondimensional variables of Section 2, Eq. (19) becomes:

$$\frac{\partial^4 w}{\partial x^4}\mathrm{d}x + \frac{\partial^2 w}{\partial t^2}\mathrm{d}x + \frac{m_p}{\rho bhl}\delta_{x_0}(x)\frac{\partial^2 w}{\partial t^2} = 0. \tag{20}$$

Let $m = m_p/\rho bhl$. Assuming that eigenmodes are unchanged with an added mass, then $\phi^m(x) = \phi^0(x) = \phi(x)$. Expressing the displacement as $w(x,t) = \phi^m(x)a^m(t) = \phi(x)a^m(t)$, Eq. (20) becomes for the i^{th} mode:

$$\frac{\mathrm{d}x}{\mathrm{d}x + m\delta_{x_0}(x)} \times \frac{1}{\phi_i(x)} \times \frac{\mathrm{d}^4\phi_i(x)}{\mathrm{d}x^4} = -\frac{1}{a_i^m(t)}\frac{\mathrm{d}^2 a_i^m(t)}{\mathrm{d}t^2} = (\omega_i^m)^2 \tag{21}$$

So:

$$\phi_i^{(IV)}(x)\mathrm{d}x - (\omega_i^m)^2\phi_i(x)\mathrm{d}x - m(\omega_i^m)^2\delta_{x_0}(x)\phi_i(x) = 0. \tag{22}$$

Without added mass, let:

$$\phi_i^{(IV)}(x) = (\omega_i^0)^2\phi_i(x), \tag{23}$$

be replaced in Eq. (22). Multiplying this equation by $\phi_i(x)$, integrating from $x = 0$ to $x = 1$, and using the normalization condition:

$$\int_0^1 \phi_i(x)^2\mathrm{d}x = 1, \tag{24}$$

we obtain:

$$\frac{(\omega_i^0)^2 - (\omega_i^m)^2}{(\omega_i^m)^2} = m\phi_i(x_0)^2. \tag{25}$$

This can be rewritten as follows by introducing $\Delta\omega_i = \omega_i^m - \omega_i^0$:

$$\frac{\Delta\omega_i}{\omega_i^0} = -\frac{1}{2}m\phi_i(x_0)^2 \tag{26}$$

Produit par HAL - 16 Sep 2014